Architectures for long-distance quantum teleportation

Jeffrey H Shapiro

Department of Electrical Engineering and Computer Science and Research Laboratory of Electronics, Massachusetts Institute of Technology, Cambridge, MA 02139, USA
E-mail: jhs@mit.edu

Abstract. A system architecture for achieving long-distance, high-fidelity teleportation and long-duration quantum storage is proposed. It uses polarization-entangled photons and trapped-atom quantum memories and is compatible with transmission over standard telecommunication fibre. An extension of this architecture permits long-distance transmission and storage of Greenberger–Horne–Zeilinger states.

1. Introduction

The preeminent obstacle to the development of quantum information technology is the difficulty of transmitting quantum information over noisy and lossy quantum communication channels, recovering and refreshing the quantum information that is received and then storing it in a reliable quantum memory. A team of researchers from the Massachusetts Institute of Technology and Northwestern University (MIT/NU) is developing a singlet-based teleportation system [1] that uses a novel ultrabright source of polarization-entangled photon pairs [2], and a trapped-atom quantum memory [3] whose loading can be nondestructively verified and whose structure permits all four Bell-state measurements to be performed. This paper reviews the primitives for the MIT/NU architecture. A loss-limited-performance analysis shows that this architecture can achieve a throughput of nearly 500 entangled pairs s^{-1} with 95% fidelity over a 50 km path when there is 10 dB of fixed loss in the overall system and 0.2 dB km^{-1} of propagation loss in the fibre. An additional primitive—the type-II degenerate optical parametric amplifier (OPA)—is then introduced. This source, which is less complicated than the dual-OPA arrangement from [2], is somewhat less effective in long-distance singlet-state teleportation. It can be used, however, within the MIT/NU architecture to perform long-distance transmission and storage of Greenberger–Horne–Zeilinger (GHZ) states via an alerted detection system akin to that in [4].
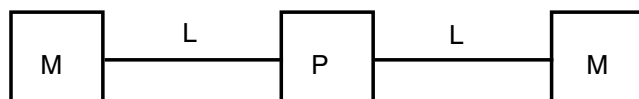
Figure 1. Schematic of long-distance quantum communication system: $P =$ ultrabright narrowband source of polarization-entangled photon pairs; $L = L$ km of standard telecommunication fibre; $M =$ trapped-atom quantum memory.

The addition of a heralded single-photon source primitive can be used to both eliminate the need for alerted detection in this GHZ-state transmission scheme, and to greatly increase its throughput.

The development of reliable, high-fidelity teleportation systems will enable networking of quantum processors over macroscopic distances. Likewise, the development of a reliable, high-fidelity distribution system for GHZ states will enable quantum secret sharing protocols [5] to be used over macroscopic distances. The architectures described in this paper, although quite challenging for experimental realization, are nevertheless promising starting points for bringing these and other quantum communication applications to fruition.

2. Long-distance teleportation

The notion that singlet states could be used to achieve teleportation is due to Bennett *et al* [6]. The transmitter and receiver stations share the entangled qubits of a singlet state, $|\psi^-\rangle_{TR} = (|0\rangle_T|1\rangle_R - |1\rangle_T|0\rangle_R)/\sqrt{2}$, and the transmitter then accepts an input-mode qubit, $|\Psi\rangle_{in} = \alpha|0\rangle_{in} + \beta|1\rangle_{in}$, leaving the input mode, transmitter and receiver in the joint state $|\Psi\rangle_{in}|\psi^-\rangle_{TR}$. Making the Bell-state measurements, $\{|\psi^\pm\rangle_{inT} = (|1\rangle_{in}|0\rangle_T \pm |0\rangle_{in}|1\rangle_T)/\sqrt{2}$, $|\phi^\pm\rangle_{inT} = (|1\rangle_{in}|1\rangle_T \pm |0\rangle_{in}|0\rangle_T)/\sqrt{2}\}$, on the joint input-mode/transmitter system then yields the two bits of classical information that the receiver needs to reconstruct the input state. An initial experimental demonstration of teleportation using singlet states was performed by Bouwmeester *et al* [7, 8], but only one of the Bell states was measured, the demonstration was a table-top experiment and it did not include a quantum memory. Our proposal for a singlet-based quantum communication system, which is shown in figure 1, remedies all of these limitations.

An ultrabright narrowband source of polarization-entangled photon pairs [2] launches the entangled qubits from a singlet state into two L km long standard telecommunication fibres. The photons emerging from the fibres are then loaded into trapped-atom quantum memories [3]. These memories store the photon-polarization qubits in long-lived hyperfine levels. Because it is compatible with fibre-optic transmission, this configuration is capable of long-distance teleportation. Because of the long decoherence times that can be realized with trapped atoms, this configuration supports long-duration quantum storage. We devote the rest of this section to summarizing the basic features of our proposal.

Each M block in figure 1 is a quantum memory in which a single ultra-cold ^{87}Rb atom ($\sim$6 MHz linewidth) is confined by a CO_2-laser trap in an ultra-high-vacuum chamber with cryogenic walls within a high-finesse ($\sim$15 MHz linewidth) single-ended optical cavity. This memory can absorb a 795 nm photon, in an arbitrary polarization state, transferring the qubit from the photon to the degenerate B levels of figure 2(a) and thence to long-lived storage levels, by coherently driving the B-to-D transitions. (We are using abstract symbols here for the hyperfine
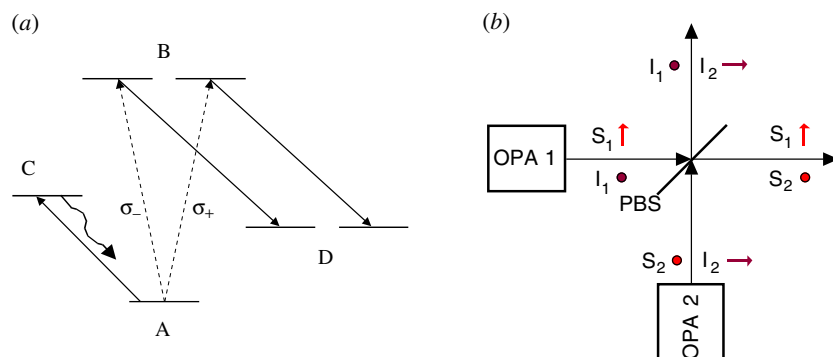
Figure 2. Essential components of the singlet-state quantum communication system from figure 1. (*a*) Simplified atomic-level schematic diagram of the trapped rubidium atom quantum memory: A-to-B transition occurs when one photon from an entangled pair is absorbed; B-to-D transition is coherently driven to enable storage in the long-lived D levels; A-to-C cycling transition permits nondestructive determination of when a photon has been absorbed. (*b*) Ultrabright narrowband source of polarization-entangled photon pairs: each optical parametric amplifier (OPAs 1 and 2) is type-II phase matched; for each optical beam the propagation direction is $\hat{z}$, and $\hat{x}$ and $\hat{y}$ polarizations are denoted by arrows and bullets, respectively; PBS, polarizing beam splitter.

levels of rubidium, see [3] for the actual atomic levels involved as well as a complete description of the memory and its operation.) With a liquid helium cryostat, so that the background pressure is less than 10^{-14} Torr, the expected lifetime of the trapped rubidium atom will be more than an hour. Fluctuations in the residual magnetic field, however, will probably limit the atom's decoherence time to a few minutes. By using optically off-resonant Raman (OOR) transitions, the Bell states of two atoms in a single vacuum-chamber trap can be converted to superposition states of one of the atoms. All four Bell measurements can then be made, sequentially, by detecting the presence (or absence) of fluorescence as an appropriate sequence of OOR laser pulses is applied to the latter atom [3]. The Bell-measurement results in one memory can be sent to a distant memory, where at most two additional OOR pulses are needed to complete the Bennett *et al* state transformation. The qubit stored in a trapped rubidium atom can be converted back into a photon by reversing the Raman excitation process that occurs during memory loading.

The P-block in figure 1 is an ultrabright narrowband source of polarization-entangled photon pairs, capable of producing $\sim 10^6$ pairs s^{-1} in ~ 30 MHz bandwidth by appropriately combining the signal and idler output beams from two doubly resonant type-II phase-matched OPAs, as sketched in figure 2(*b*) [2]. The fluorescence spectrum of the signal and idler beams is controlled by the doubly resonant OPA cavities. These can be advantageously and easily tailored to produce the desired (factor-of-two broader than the memory-cavity's) bandwidth. By using periodically poled potassium titanyl phosphate (PPKTP), a quasi-phase-matched type-II nonlinear material, we can produce $\sim 10^6$ pairs s^{-1} at the 795 nm wavelength of the rubidium memory for direct memory-loading (i.e. local-storage) applications. For long-distance transmission to remotely located memories, we use a different PPKTP crystal and pump wavelength to generate $\sim 10^6$ pairs s^{-1} in the 1.55 μm wavelength low-loss fibre transmission window. After fibre propagation we then shift the entanglement to the 795 nm wavelength

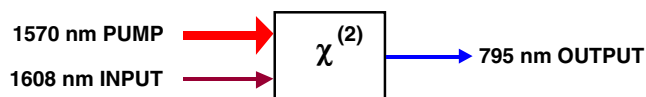Institute *of* **Physics** 🔷 DEUTSCHE PHYSIKALISCHE GESELLSCHAFT

Figure 3. Schematic diagram of quantum frequency conversion: a strong pump beam at 1570 nm converts a qubit photon received at 1608 nm (in the low-loss fibre transmission window) to a qubit photon at the 795 nm wavelength of the ^{87}Rb quantum memory.

needed for the rubidium-atom memory via quantum-state frequency translation, a procedure previously proposed and demonstrated by Kumar [9, 10] and shown schematically in figure 3. For our application, we expect that 80% conversion efficiency should be obtainable by placing a 5 cm long periodically poled lithium niobate (PPLN) crystal inside a cavity that resonates the 1570 nm, but not the 1608 or 795 nm light, and using 0.5 W of pump power.

Successful singlet transmission requires that polarization not be degraded by the propagation process. Because we are concerned with the transmission of very weak, narrowband light fields, it is only the slowly varying birefringence of installed fibre that must be dealt with; i.e. polarization-mode dispersion, guided acoustic-wave Brillouin scattering and the like need not be considered. Our scheme for polarization maintenance, shown schematically in figure 4, relies on time-division multiplexing. Time slices (say 400 ns long) from the signal beams from our two OPAs are sent down one fibre in the same linear polarization but in nonoverlapping (say 200 ns separation) time slots, accompanied by a strong out-of-band laser pulse. By tracking and restoring the linear polarization of the strong pulse, we can restore the linear polarization of the signal-beam time slices at the far end of the fibre. After this linear-polarization restoration, we then reassemble a time-epoch of the full vector signal beam by delaying the first time slot and combining it on a polarizing beam splitter with the second time slot after the latter has had its linear polarization rotated by 90°. A similar procedure is performed to reassemble idler time-slices after they have propagated down the other fibre in figure 1. This approach, which is inspired by the Bergman *et al* two-pulse fibre-squeezing experiment [11], common-modes out the vast majority of the phase fluctuations and the polarization birefringence incurred in the fibre, permitting standard telecommunication fibre to be used in lieu of the lossier and much more expensive polarization-maintaining fibre.

3. Loss-limited performance

Quantum communication is carried out in the figure 1 configuration via the following protocol. The entire system is clocked. Time slots of signal and idler (say 400 ns long) are transmitted down optical fibres to the quantum memories. These slots are gated into the memory cavities— with their respective atoms either physically displaced or optically detuned so that no A-to-B (i.e. no 795 nm) absorptions occur. After a short loading interval (a few cold-cavity lifetimes, say 400 ns), each atom is moved (or tuned) into the absorbing position and B-to-D coherent pumping is initiated. After about 100 ns, coherent pumping ceases and the A-to-C cycling transition (shown in figure 2(a)) is repeatedly driven (say 30 times, taking nearly 1 μs). By monitoring a cavity for the fluorescence from this cycling transition, we can reliably detect whether or not a 795 nm photon has been absorbed by the atom in that cavity. If neither atom or if only one atom has absorbed such a photon, then we cycle both atoms back to their A states and
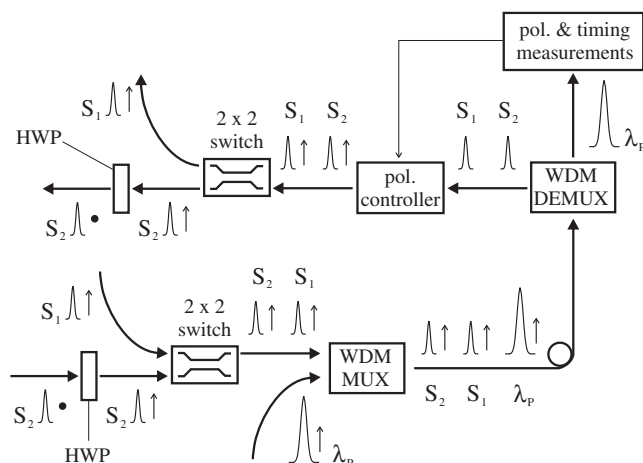
Figure 4. Transmission of time-division multiplexed signal beams from OPAs 1 and 2 through an optical fibre. With the use of a half-wave plate (HWP) the signal pulses and the pilot pulse are linearly polarized the same way. The pilot pulse—at a wavelength λ_p which is different from the signal or idler wavelengths—is injected into and extracted from the fibre using a wavelength-division multiplexer (WDM MUX) and a wavelength-division demultiplexer (WDM DEMUX), respectively. Not shown is the final polarizing beam splitter for combining the two signal-beam outputs, cf figure 2(*b*). A similar overall arrangement is used to transmit the idler beams from OPAs 1 and 2.

start anew. If no cycling-transition fluorescence is detected in either cavity, then, because we have employed enough cycles to ensure very high probability of detecting that the atom is in its A state, it must be that both atoms have absorbed 795 nm photons and stored the respective qubit information in their long-lived degenerate D levels. These levels are not resonant with the laser driving the cycling transition, and so the loading of our quantum memory is nondestructively verified in this manner.

We expect that the preceding memory-loading protocol can be run at rates as high as $R = 500$ kHz; i.e., we can get an independent try at loading an entangled photon pair into the two memory elements of figure 1 every 2 μs. With a high probability, P_{erasure}, any particular memory-loading trial will result in an erasure, i.e. propagation loss and other inefficiencies combine to preclude both atoms from absorbing photons in the same time epoch. With a low probability, P_{success}, the two atoms will absorb the photons from a single polarization-entangled pair, namely, we have a memory-loading success. With a much lower probability, P_{error}, both atoms will have absorbed photons but these photons will not have come from a single polarization-entangled pair; this is the error event.

There are two key figures-of-merit for the figure 1 configuration: throughput and fidelity. Propagation losses and other inefficiencies merely increase P_{erasure} and hence reduce the throughput, i.e. the number of successful entanglement-loadings/s, $N_{\text{success}} \equiv RP_{\text{success}}$, that could be achieved if the quantum memories each contained a lattice of trapped atoms for sequential loading of many pairs. Loading errors, which occur with probability P_{error}, provide the ultimate limit on the teleportation fidelity that can be realized with the figure 1 architecture. This loss-limited teleportation fidelity is defined by $F_{\text{max}} \equiv {}_{\text{out}}\langle\Psi|\hat{\rho}_{\text{out}}|\Psi\rangle_{\text{out}}$,

where $|\Psi\rangle_{\text{out}} = \alpha|0\rangle_{\text{out}} + \beta|1\rangle_{\text{out}}$ is the output state that is obtained from perfect teleportation of $|\Psi\rangle_{\text{in}}$, and $\hat{\rho}_{\text{out}}$ is the density operator for the actual (mixed) state that results from the teleportation process. Note that $\hat{\rho}_{\text{out}}$ is a conditional density operator, in that teleportation is only attempted when both memories have absorbed photons. We assume, in computing $F_{\max}$, that perfect Bell-state measurements and post-measurement state transformation are made, so that a loading success yields fidelity 1. We shall assume that the error event loads independent, randomly polarized photons into each memory, from which uniform Bloch-sphere averaging shows that a loading error yields fidelity $1/2$. Combining these results we have that $F_{\max} = 1 - P_{\text{error}}/2(P_{\text{success}} + P_{\text{error}})$, for the loss-limited teleportation fidelity of the figure 1 architecture.

3.1. OPA statistics

Assume matched signal and idler cavities, each with linewidth Γ, zero detuning and no excess loss. Also assume anti-phased pumping at a fraction, G^2, of oscillation threshold, with no pump depletion or excess noise. From [2] we then have that the output beams from OPAs 1 and 2 are in an entangled, zero-mean Gaussian pure state, which is completely characterized by the following normally ordered and phase-sensitive correlation functions:

$$\langle \hat{A}^{\dagger}_{k_j}(t+\tau)\hat{A}_{k_j}(t)\rangle = \frac{G\Gamma}{2}\left[\frac{\mathrm{e}^{-(1-G)\Gamma|\tau|}}{1-G} - \frac{\mathrm{e}^{-(1+G)\Gamma|\tau|}}{1+G}\right], \tag{1}$$

$$\langle \hat{A}_{S_j}(t+\tau)\hat{A}_{I_j}(t)\rangle = \frac{(-1)^{j-1}G\Gamma}{2}\left[\frac{\mathrm{e}^{-(1-G)\Gamma|\tau|}}{1-G} + \frac{\mathrm{e}^{-(1+G)\Gamma|\tau|}}{1+G}\right], \tag{2}$$

where $\{\hat{A}_{k_j}(t)\mathrm{e}^{-i\omega_k t} : k = S \text{ (signal)}, I \text{ (idler)}, j = 1, 2\}$ are positive-frequency, photon-units OPA-output field operators.

After combining the outputs of OPAs 1 and 2 into vector fields $\hat{\boldsymbol{A}}_S(t)$ and $\hat{\boldsymbol{A}}_I(t)$, we can show that the Fourier component of the vector-signal field at frequency $\omega_S + \Delta\omega$ and the vector-idler Fourier component at frequency $\omega_I - \Delta\omega$ are in the entangled Bose–Einstein state,

$$|\psi\rangle_{SI} = \sum_{n=0}^{\infty}\sqrt{\frac{\bar{N}^n}{(\bar{N}+1)^{n+1}}}|n\rangle_{S_x}|n\rangle_{I_y} \sum_{n=0}^{\infty}(-1)^n\sqrt{\frac{\bar{N}^n}{(\bar{N}+1)^{n+1}}}|n\rangle_{S_y}|n\rangle_{I_x} \tag{3}$$

in number–ket representation, where $\bar{N} = 4G^2/[(1-G^2-\Delta\omega^2/\Gamma^2)^2 + 4\Delta\omega^2/\Gamma^2]$ is the average photon number per mode at detuning $\Delta\omega$. For $\bar{N} \ll 1$, this joint state reduces to

$$|\psi\rangle_{SI} \approx \frac{1}{\bar{N}+1}|0\rangle_{S_x}|0\rangle_{I_y}|0\rangle_{S_y}|0\rangle_{I_x}$$

$$+ \sqrt{\frac{\bar{N}}{(\bar{N}+1)^3}}(|1\rangle_{S_x}|1\rangle_{I_y}|0\rangle_{S_y}|0\rangle_{I_x} - |0\rangle_{S_x}|0\rangle_{I_y}|1\rangle_{S_y}|1\rangle_{I_x}), \tag{4}$$

i.e. it is predominantly vacuum, augmented by a small amount of the singlet state, $|\psi^-\rangle_{\text{TR}} = (|0\rangle_{\text{T}}|1\rangle_{\text{R}} - |1\rangle_{\text{T}}|0\rangle_{\text{R}})/\sqrt{2}$, with $|0\rangle_{\text{T}} \equiv |1\rangle_{S_x}|0\rangle_{Sy}$, $|1\rangle_{\text{T}} \equiv |0\rangle_{S_x}|1\rangle_{S_y}$, $|0\rangle_{\text{R}} \equiv |1\rangle_{I_x}|0\rangle_{I_y}$ and $|1\rangle_{\text{R}} \equiv |0\rangle_{I_x}|1\rangle_{I_y}$.

The presence of excess loss within the OPA cavities, and/or propagation loss along the fibre can be incorporated into this OPA analysis in a straightforward manner [12]. Assuming symmetric operation, in which the signal and idler encounter identical intracavity and fibre losses, then the correlation-function formulae, equations (1) and (2), are merely multiplied by $\eta_L\gamma/\Gamma$,

where $\eta_L < 1$ is the transmission through the fibre and $\gamma < \Gamma$ is the output-coupling rate of the OPA cavity.

3.2. Cavity-loading statistics

The internal annihilation operators of the quantum memory cavities—over the T_c s long loading interval—are related to the incoming signal and idler field operators as follows:

$$\hat{\boldsymbol{a}}_k(T_c) = \hat{\boldsymbol{a}}_k(0)\mathrm{e}^{-\Gamma_c T_c} + \int_0^{T_c} \mathrm{d}t\, \mathrm{e}^{-\Gamma_c(T_c-t)}\Big[\sqrt{2\gamma_c}\hat{\boldsymbol{A}}_k(t) + \sqrt{2(\Gamma_c-\gamma_c)}\hat{\boldsymbol{A}}_{k_v}(t)\Big], \tag{5}$$

for $k = S, I$, where $\gamma_c < \Gamma_c$ is the input-coupling rate and Γ_c is the linewidth of the (assumed to be identical for signal and idler) memory cavities. The initial intracavity operators and the loss-operators, $\{\hat{\boldsymbol{a}}_k(0), \hat{\boldsymbol{A}}_{k_v}(t)\}$, are in vacuum states.

It is now easy to show that the joint density operator (state) for $\{\hat{\boldsymbol{a}}_S(T_c), \hat{\boldsymbol{a}}_I(T_c)\}$, takes the factored form, $\hat{\rho}_{SI} = \hat{\rho}_{S_x I_y}\hat{\rho}_{S_y I_x}$, where the two-mode density operators on the right-hand side are Gaussian mixed states given by the anti-normally ordered characteristic functions,

$$\chi_A^{\rho_{S_x I_y}}(\boldsymbol{\zeta}^*, \boldsymbol{\zeta}) \equiv \mathrm{tr}\big[\hat{\rho}_{S_x I_y}\mathrm{e}^{-\zeta_S^* \hat{a}_{S_x} - \zeta_I^* \hat{a}_{I_y}}\mathrm{e}^{\zeta_S \hat{a}_{S_x}^\dagger + \zeta_I \hat{a}_{I_y}^\dagger}\big] = \mathrm{e}^{-(1+\bar{n})(|\zeta_S|^2+|\zeta_I|^2)+2\tilde{n}\,\mathrm{Re}\,(\zeta_S\zeta_I)}, \tag{6}$$

and

$$\chi_A^{\rho_{S_y I_x}}(\boldsymbol{\zeta}^*, \boldsymbol{\zeta}) \equiv \mathrm{tr}\big[\hat{\rho}_{S_y I_x}\mathrm{e}^{-\zeta_S^* \hat{a}_{S_y} - \zeta_I^* \hat{a}_{I_x}}\mathrm{e}^{\zeta_S \hat{a}_{S_y}^\dagger + \zeta_I \hat{a}_{I_x}^\dagger}\big] = \mathrm{e}^{-(1+\bar{n})(|\zeta_S|^2+|\zeta_I|^2)-2\tilde{n}\,\mathrm{Re}\,(\zeta_S\zeta_I)}, \tag{7}$$

where $\bar{n} \equiv I_- - I_+$ and $\tilde{n} \equiv I_- + I_+$, with $I_\mp \equiv \eta_L\gamma\gamma_c G/\Gamma_c(1\mp G)[(1\mp G)\Gamma + \Gamma_c]$.

3.3. Throughput and fidelity calculations

From the loaded-cavity state we can find the erasure, success and error probabilities via

$$\begin{aligned} P_{\mathrm{erasure}} = {}&(_{S_x}\langle 0|\hat{\rho}_{S_x}|0\rangle_{S_x})(_{S_y}\langle 0|\hat{\rho}_{S_y}|0\rangle_{S_y}) + (_{I_x}\langle 0|\hat{\rho}_{I_x}|0\rangle_{Ix})(_{I_y}\langle 0|\hat{\rho}_{I_y}|0\rangle_{I_y}) \\ &- (_{S_x}\langle 0|_{I_y}\langle 0|\hat{\rho}_{S_x I_y}|0\rangle_{I_y}|0\rangle_{S_x})(_{S_y}\langle 0|_{I_x}\langle 0|\hat{\rho}_{S_y I_x}|0\rangle_{I_x}|0\rangle_{S_y}), \end{aligned} \tag{8}$$

$$P_{\mathrm{success}} = {}_{SI}\langle\psi^-|\hat{\rho}_{\boldsymbol{SI}}|\psi^-\rangle_{SI} \tag{9}$$

$$P_{\mathrm{error}} = 1 - P_{\mathrm{erasure}} - P_{\mathrm{success}}, \tag{10}$$

where $|\psi^-\rangle_{SI} \equiv (|1\rangle_{S_x}|1\rangle_{I_y}|0\rangle_{S_y}|0\rangle_{I_x} - |0\rangle_{S_x}|0\rangle_{I_y}|1\rangle_{S_y}|1\rangle_{I_x})/\sqrt{2}$ is the singlet state. In the appendix we shall derive explicit expressions for the erasure and success probabilities, starting from the anti-normally ordered characteristic functions given in section 3.2. Note that the atom–field coupling is not explicitly treated in this analysis. The erasure and success probabilities are obtained from the cold-cavity loading theory; inefficiency in the actual atom–field coupling can be included, in this analysis, as a fixed (path-length-independent) loss in source-to-memory transmission.

In figure 5 we have plotted the throughput, N_{success}, and the loss-limited fidelity, F_{max}, of our quantum communication system under the following operating conditions: dual-OPA (figure 2(b)) source with each OPA operated at 1% of its oscillation threshold ($G^2 = 0.01$), 5 dB of excess loss in each P-to-M block path in figure 1; 0.2 dB km^{-1} loss in each fibre; $\Gamma_c/\Gamma = 0.5$ ratio of memory-cavity linewidth to source-cavity linewidth and $R = 500$ kHz memory cycling rate. We see from this figure that a throughput of nearly 200 pairs s^{-1} is achieved at an end-to-end path length ($2L$) of 50 km with a loss-limited teleportation fidelity in excess of 97%.
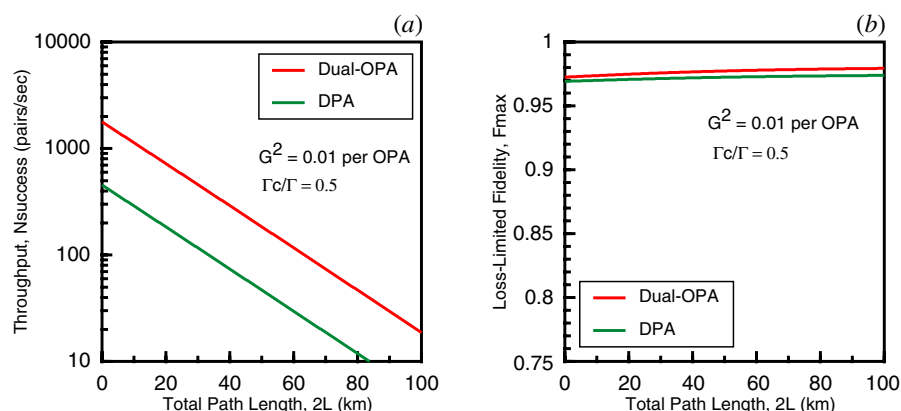
Figure 5. Figures of merit for the figure 1 architecture for dual-OPA and degenerate parametric amplifier (DPA) source configurations. (*a*) Throughput, N_{success}, versus total path length, $2L$. (*b*) Loss-limited teleportation fidelity, F_{max}, versus total path length, $2L$. All curves assume OPAs operating at 1% of their oscillation thresholds, 5 dB of excess loss per P-to-M block connection, $0.2\,\text{dB}\,\text{km}^{-1}$ fibre-propagation loss, $\Gamma_c/\Gamma = 0.5$ ratio of memory-cavity linewidth to source-cavity linewidth and $R = 500\,\text{kHz}$ memory cycling rate.

4. Teleportation with a degenerate parametric amplifier

The singlet-state teleportation architecture that we have just described relies on a pair of coherently pumped OPAs for its entangled photons. It turns out that a simpler source arrangement offers comparable quantum communication performance. Consider the doubly resonant, type-II phase-matched DPA shown schematically in figure 6. Operated at degeneracy, the centre frequencies of the signal and idler beams exiting the OPA cavity are both equal to $\omega_P/2$, i.e. half the OPA's pump frequency. Because the OPA produces signal and idler photons in pairs, and the members of each pair are distinguishable only because of their orthogonal polarizations, the $50/50$ beam splitter in figure 6 yields output beams containing a triplet-state component. In particular, when a signal/idler pair encounters this beam splitter there is a $50/50$ chance that one photon will appear in each output port. When this occurs, a symmetry argument shows that the joint output state from the $50/50$ beam splitter is the triplet state $|\psi^+\rangle_{SI} \equiv (|1\rangle_{S_x}|1\rangle_{I_y}|0\rangle_{S_y}|0\rangle_{I_x} + |0\rangle_{S_x}|0\rangle_{I_y}|1\rangle_{S_y}|1\rangle_{I_x})/\sqrt{2}$. (An initial DPA experiment [13] has yielded a pair flux that is 10^4 times brighter, per unit bandwidth per unit pump power, than the best parametric downconverter result from the literature. This experiment also provided preliminary quantum-interference evidence of triplet-state generation.) Although the Bennett *et al* teleportation protocol usually presumes that a singlet is shared by its transmitter and receiver, a simple modification can be made so that the triplet state $|\psi^+\rangle_{SI}$ can be used in lieu of the singlet $|\psi^-\rangle_{SI}$. Alternatively, the phase of the signal-beam's $\hat{y}$ polarization can be flipped by placing an HWP after the $50/50$ beam splitter, thus converting $|\psi^+\rangle_{SI}$ to $|\psi^-\rangle_{SI}$.

If the degenerate-OPA arrangement from figure 6 is used as the source block in the figure 1 architecture, the OPA statistics, cavity-loading statistics and throughput/fidelity calculations from section 3 can easily be adapted to this new configuration. In particular, the joint density operator
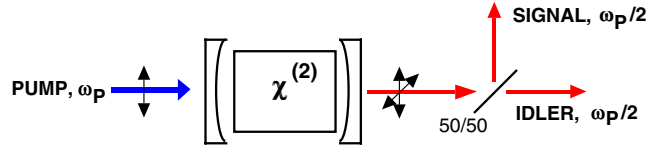
Figure 6. Doubly resonant, type-II phase-matched degenerate OPA. Signal and idler photons emerge in frequency-degenerate, orthogonally polarized pairs from the OPA cavity. The joint state of the beams exiting the $50/50$ beam splitter is mixed, but includes a triplet component that can be used as the entanglement source in the figure 1 teleportation architecture.

for $\{\hat{\boldsymbol{a}}_S(T_c), \hat{\boldsymbol{a}}_I(T_c)\}$ is a Gaussian mixed state that is given by the following anti-normally ordered characteristic function:

$$
\begin{aligned}
\chi_A^{\rho_{S_x I_x S_y I_y}}(\boldsymbol{\zeta}^*, \boldsymbol{\zeta}) &= \mathrm{tr}[\hat{\rho}_{S_x I_x S_y I_y} \mathrm{e}^{-\zeta_{S_x}^* \hat{a}_{S_x} - \zeta_{I_x}^* \hat{a}_{I_x} - \zeta_{S_y}^* \hat{a}_{S_y} - \zeta_{I_y}^* \hat{a}_{I_y}} \mathrm{e}^{\zeta_{S_x} \hat{a}_{S_x}^\dagger + \zeta_{I_x} \hat{a}_{I_x}^\dagger + \zeta_{S_y} \hat{a}_{S_y}^\dagger + \zeta_{I_y} \hat{a}_{I_y}^\dagger}] \\
&= \mathrm{e}^{-(1+\bar{n})(|\zeta_{S_x} + \zeta_{I_x}|^2 + |\zeta_{S_y} + \zeta_{I_y}|^2)/2 + \tilde{n}\, \mathrm{Re}\,[(\zeta_{S_x} + \zeta_{I_x})(\zeta_{S_y} + \zeta_{I_y})]} \\
&\quad \times \mathrm{e}^{-(|\zeta_{S_x} - \zeta_{I_x}|^2 + |\zeta_{S_y} - \zeta_{I_y}|^2)/2},
\end{aligned}
\tag{11}
$$

where $\bar{n} \equiv I_- - I_+$ and $\tilde{n} \equiv I_- + I_+$, with $I_\mp \equiv \eta_L \gamma \gamma_c G / \Gamma_c (1 \mp G)[(1 \mp G)\Gamma + \Gamma_c]$, as before. Using this density operator, the erasure probability for the degenerate-OPA quantum communication systems is found via

$$
\begin{aligned}
P_{\mathrm{erasure}} &= ({}_{S_x}\langle 0|\, {}_{S_y}\langle 0| \hat{\rho}_{S_x S_y} |0\rangle_{S_y} |0\rangle_{S_x}) + ({}_{I_x}\langle 0|\, {}_{I_y}\langle 0| \hat{\rho}_{I_x I_y} |0\rangle_{I_y} |0\rangle_{I_x}) \\
&\quad - ({}_{S_x}\langle 0|\, {}_{I_x}\langle 0|\, {}_{S_y}\langle 0|\, {}_{I_y}\langle 0| \hat{\rho}_{S_x I_x S_y I_y} |0\rangle_{I_y} |0\rangle_{S_y} |0\rangle_{I_x} |0\rangle_{S_x}),
\end{aligned}
\tag{12}
$$

its success probability is calculated from $P_{\mathrm{success}} = {}_{SI}\langle \psi^+ | \hat{\rho}_{\boldsymbol{SI}} | \psi^+ \rangle_{SI}$ and its error probability is obtained from the closure relation, $P_{\mathrm{error}} = 1 - P_{\mathrm{erasure}} - P_{\mathrm{success}}$. Throughput and fidelity results follow directly from these probabilities and the memory cycling rate, just at they did for the dual-OPA source case that was treated in section 3: for the DPA source we have that $N_{\mathrm{success}} = R P_{\mathrm{success}}$ and $F_{\mathrm{max}} = 1 - P_{\mathrm{error}}/2(P_{\mathrm{success}} + P_{\mathrm{error}})$, where we have again assumed that the error event loads independent, randomly polarized photons into each memory. In the appendix we shall derive explicit results for the success and error probabilities starting from the anti-normally ordered characteristic function given in equation (11).

Figure 5 compares the throughputs and loss-limited fidelities of the dual-OPA and the degenerate OPA teleportation systems when the OPAs are operated at 1% of oscillation threshold ($G^2 = 0.01$), there is 5 dB of excess loss in each P-to-M block path in figure 1 and 0.2 dB km^{-1} loss in each fibre, the ratio of memory-cavity linewidth to source-cavity linewidth is 0.5 ($\Gamma_c/\Gamma = 0.5$) and the memory cycling rate is $R = 500$ kHz. At this pumping level the dual-OPA source supports a throughput of nearly 200 pairs s^{-1} out to a 50 km end-to-end span with 97.7% fidelity, whereas the degenerate-OPA source achieves only about 50 pairs s^{-1} at a slightly lower fidelity over this same span. The 6 dB difference between the dual-OPA and degenerate-OPA throughputs is easily explained. The degenerate-OPA configuration has half the raw flux of the dual-OPA system, because each of the latter's individual OPAs is pumped at 1% of threshold. The degenerate OPA suffers an additional factor-of-two loss, relative to the dual-OPA setup, because of the $50/50$ beam splitter in figure 6. Specifically, the full flux of the dual-OPA setup is losslessly combined by the polarizing beam splitter in figure 2(*b*), whereas half the time both photons emerge from the same output port of the degenerate-OPA configuration's $50/50$ beam splitter thus precluding formation of the triplet state needed for a loading success.
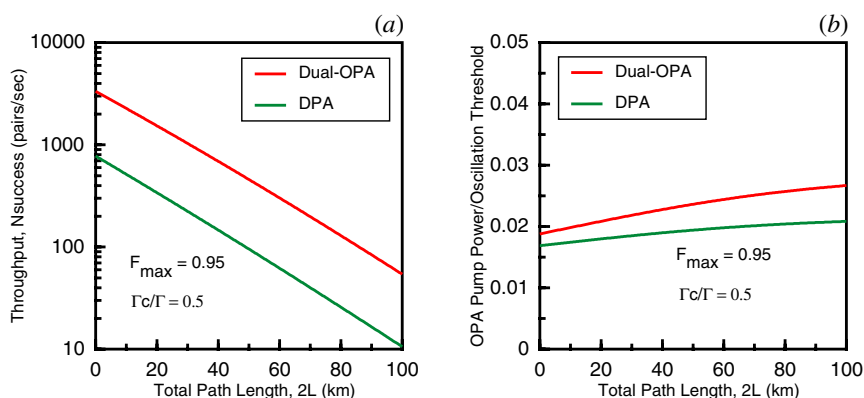
Figure 7. Gain-optimized performance of the figure 1 architecture for dual-OPA and DPA source configurations. (*a*) Throughput, N_{success}, versus total path length, $2L$. (*b*) Normalized OPA gain, G^2, versus total path length, $2L$. All curves assume 5 dB of excess loss per P-to-M block connection, 0.2 dB km^{-1} fibre-propagation loss, $\Gamma_c/\Gamma = 0.5$ ratio of memory-cavity linewidth to source-cavity linewidth and $R = 500$ kHz memory cycling rate.

Figure 7(*a*) compares the throughputs of the dual-OPA and degenerate OPA teleportation systems when, for every path length, the OPA gain is adjusted to maximize N_{success} under the fidelity constraint $F_{\text{max}} = 0.95$ with the other parameter values remaining as they were for figure 5. Figure 7(*b*) shows the G^2 values needed to obtain these gain-optimized throughputs. Comparison of the dual-OPA throughput curve in figure 7(*a*) with the one shown in figure 5(*a*) reveals the value of OPA gain optimization. At 50 km total path length, throughput is increased by a factor of two by increasing OPA pumping from 1 to 2.3%. The price paid for this throughput increase is a decrease in fidelity from 97.7 to 95%. For the DPA source, OPA gain optimization affords a factor of two increase in throughput at 50 km total path length by increasing the OPA gain from 1 to 1.9%. This gain increase also decreases the fidelity, at 50 km total path length, from 97.2 to 95%. Note that after gain optimization, the dual-OPA system continues to outperform the DPA system by about 6 dB in throughput. In our throughput/fidelity analysis—which neglects all propagation effects other than loss, and assumes perfect Bell-state measurements and teleportation state transformation—the fidelity falls below one because our sources can produce more than one pair in a loading interval. In order to meet the 95% fidelity constraint, the parametric-amplifier gains in both our dual-OPA and DPA architectures must be kept low enough to ensure that multiple-pair events do not reduce teleportation fidelity to an unacceptable level. As a result, the DPA system is unable to recoup its 6 dB throughput disadvantage by increasing its pumping level to four times that of each OPA in the figure 2(*b*) setup.

5. GHZ-state communication

Singlet-state teleportation relies on two-particle entanglement. There is considerable interest currently in N-party entanglement, i.e. in the generation and application of entangled states of $N > 2$ particles. Greenberger, Horne and Zeilinger showed that such multi-particle states were
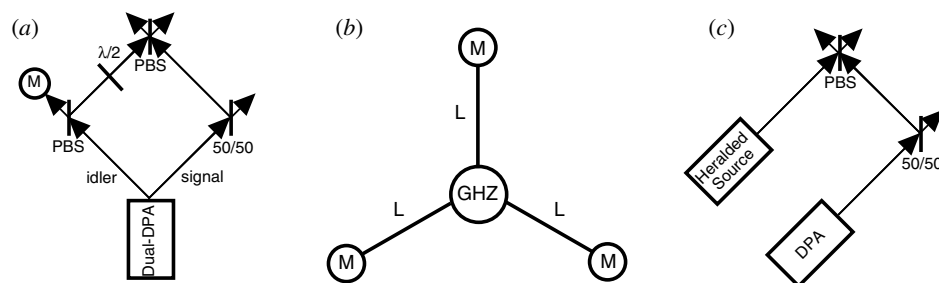
Figure 8. (*a*) DPA system for generation of GHZ states. The dual degenerate parametric amplifier (dual-DPA) is a figure 2(*b*) arrangement in which OPAs 1 and 2 operate at frequency degeneracy and are pumped in phase. PBS, polarizing beam splitter; M, trapped-Rb atom quantum memory; $\lambda/2$, HWP. (*b*) Long-distance communication architecture for GHZ states. GHZ is the source arrangement from either (*a*) or (*c*); L denotes L km of standard telecommunication fibre. (*c*) Heralded single-photon source plus DPA system for generation of GHZ states.

of fundamental importance because they led to conflicts with local realism for nonstatistical predictions of quantum mechanics [14]. The simplest state of this GHZ class, namely

$$|\psi\rangle_{\text{GHZ}} \equiv (|\uparrow\rangle|\uparrow\rangle|\bullet\rangle + |\bullet\rangle|\bullet\rangle|\uparrow\rangle)/\sqrt{2}, \tag{13}$$

has been shown, theoretically, to permit quantum secret sharing [5]. The initial experimental demonstration of GHZ-state generation by Bouwmeester *et al* [4], like their earlier work on singlet-state teleportation, was an annihilative table-top measurement. Moreover it had an extremely low flux: 1 GHZ state every 150 s. Here we will show that the MIT/NU quantum communication architecture can lead to long-distance transmission and storage of GHZ states via an alerted detection scheme akin to that in [4].

Figure 8(*a*) is a simplified redrawing of the Innsbruck group's GHZ-state source, in which we have replaced their parametric downconverter with a pair of doubly resonant, type-II phase-matched degenerate OPAs—arranged as in figure 2(*b*) to produce polarization entanglement— and we have placed a trapped-atom quantum memory at the trigger-output port of the polarizing beam splitter. Figure 8(*b*) shows the embedding of this GHZ-state source into a long-distance quantum communication architecture in which L km long spans of standard telecommunication fibre are used to connect to trapped-Rb-atom quantum memories. (As in figure 1, we have not shown the quantum frequency conversion and time-division multiplexing arrangements that are needed to make use of the 1.55 μm low-loss window and to suppress the ill effects of time-varying birefringence.) The system in figures 8(*a*), (*b*) is run under a clocked protocol similar to the one described for singlet-state transmission in section 3. In each time epoch we monitor the cycling transitions on all four quantum memories, namely the three external memories shown in figure 8(*b*) plus the fourth memory (internal to the source block in that panel) that is present in figure 8(*a*). The loading protocol is repeated until all four memories absorb photons in the same time epoch. As shown for annihilative measurements in [4], when all four memories in figures 8(*a*), (*b*) have absorbed photons, and these photons came from the emission of two entangled signal-idler pairs from the dual-DPA, then the three external memories have been loaded into the GHZ state,

$$|\psi\rangle_{\text{GHZ}} \equiv (|1\rangle_{1_y}|1\rangle_{2_y}|1\rangle_{3_x}|0\rangle_{1_x}|0\rangle_{2_x}|0\rangle_{3_y} + |0\rangle_{1_y}|0\rangle_{2_y}|0\rangle_{3_x}|1\rangle_{1_x}|1\rangle_{2_x}|1\rangle_{3_y})/\sqrt{2}, \tag{14}$$
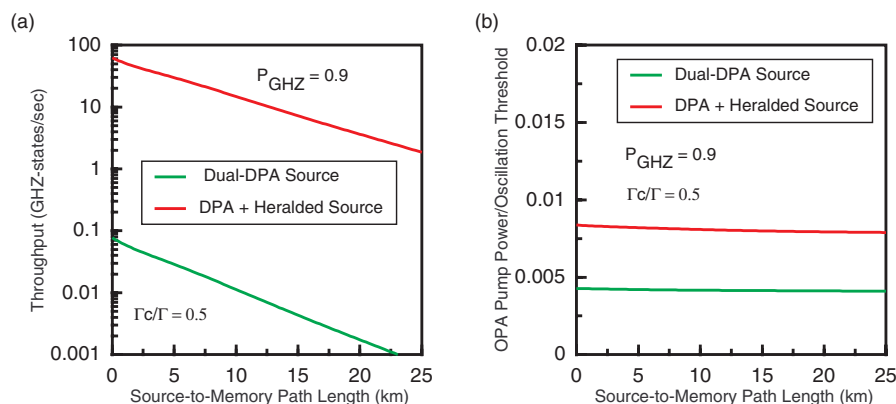
Figure 9. Gain-optimized performance for the figure 8 architecture. (*a*) GHZ-state throughput versus source-to-memory path length, L, for dual-DPA and DPA plus heralded single-photon sources. (*b*) Normalized DPA gain, G^2, versus source-to-memory path length, L. All curves assume 5 dB of excess loss per source-to-memory connection, 0.2 dB km^{-1} fibre-propagation loss, $\Gamma_c/\Gamma = 0.5$ ratio of memory-cavity linewidth to source-cavity linewidth and $R = 500$ kHz memory cycling rate.

in number–ket representation for the $\hat{x}$ and $\hat{y}$ polarizations, where $\{1, 2, 3\}$ is a clockwise labeling of the memories in figure 8(*b*) starting from the lower left.

A performance analysis of this GHZ-state communication scheme can be carried out using the OPA and cavity-loading statistics that we have described in section 3; the appendix provides some of the details. There will again be three possible outcomes for every loading trial of the figure 8(*a*), (*b*) system: an erasure occurs when one or more the four memories fails to absorb a photon; a success occurs when all four memories absorb photons and the three memories external to the source share a GHZ state; an error occurs when all four memories absorb photons, but the three external memories do not share a GHZ state. Figure 9(*a*) shows the throughput, $N_{\text{success}} = R P_{\text{success}}$, versus source-to-memory path length L when, for each L value, the DPA gain is chosen to maximize throughput subject to the constraint,

$$P_{\text{GHZ}} \equiv \frac{P_{\text{success}}}{P_{\text{success}} + P_{\text{error}}} = 0.9. \tag{15}$$

In other words, this figure shows the maximum throughput that can be achieved when the conditional probability of loading a GHZ state, given that there has not been an erasure, is 0.9. Figure 9(*b*) shows the DPA gain value needed to achieve these throughput results. The greatly reduced likelihood that a dual-DPA produces two signal–idler pairs in a loading interval— as compared with its probability of producing one such pair—is the primary reason that the GHZ-state throughput in figure 9(*a*) is so much lower than the teleportation throughputs we saw in figures 5(*a*) and 7(*a*). On the positive side, however, we see that the architecture from figures 8(*a*), (*b*) permits a throughput comparable to what Bouwmeester *et al* produced in the laboratory to be realized over a 10 km source-to-memory radius with 90% conditional probability of success. More important, though, is the fact that the memories in the figure 8 architecture allow the GHZ state to be stored for use in quantum secret sharing or other applications of three-particle entanglement.

A route to obtaining substantially higher throughputs from the figure 8(*b*) architecture may be developed by examining the role of the memory element in figure 8(*a*). Suppose that the dual DPA emits two entangled-photon pairs from which each of the memories in figures 8(*a*), (*b*) captures one photon. The polarization of the photon captured by the figure 8(*a*) memory is determined, by the polarizing beam splitter, as is the polarization of the photon entering the HWP in that figure. The HWP's orientation forces the latter photon to have a $50/50$ chance of taking either output port of the ensuing polarizing beam splitter. It then follows that the three external memories share a GHZ state. Note that the sole purpose of the figure 8(*a*) memory is to serve as a trigger, i.e. to herald (by its absorbing a photon of a definite polarization) the presence of a photon in the orthogonal polarization at the input to the HWP. Recent work has shown that it may be possible to construct heralded single-photon sources [15]. With such a source, used in the configuration shown in figure 8(*c*), there would be a single photon entering the HWP during every cycle of the loading protocol, as compared with the much lower flux that prevails in the figure 8(*a*) version of the GHZ-state source. When this heralded source produces one photon per loading interval in the proper spatio-temporal mode for coupling to the trapped-atom quantum memory, vastly improved GHZ-state communication results from using the figure 8(*c*) source in the figure 8(*b*) transmission architecture, as shown in figure 9(*a*). In particular, throughput rises by three orders of magnitude, to about 15 GHZ states s^{-1} at 10 km radius. Note that the source-to-memory radius for which GHZ-state communication can be achieved may be extended by teleporting the contents of any or all of the figure 8(*b*) memories using the long-distance teleportation architecture shown in figure 1. Thus, it should be possible to share GHZ states over long distances for use in quantum secret sharing or other multi-party entanglement protocols.

6. Discussion

We have described architectures for long-distance, high-fidelity quantum teleportation and GHZ-state transmission. Because of their nondestructive memory-loading verification, their ultrabright entanglement sources, and their ability to employ the low-loss wavelength window in standard telecommunication fibre, these systems can sustain appreciable throughputs and high fidelities over loss-limited operating ranges well beyond those of previous quantum repeater proposals. Of course, our analysis has neglected additional degradations that may arise from residual phase errors in transmission, imperfect Bell-state measurements etc, which will reduce achievable fidelities. Nevertheless, the figure 1 and 8 configurations offer substantial promise for bringing quantum communications from conditional demonstrations in the laboratory to viable system implementations.

Acknowledgments

Appendix

Here we shall sketch derivations of the success and error probabilities for the dual-OPA source and DPA source teleportation architectures, and also for the dual-DPA source and the DPA plus heralded single-photon source GHZ-state architectures.

A.1. Dual-OPA source teleportation

The anti-normally ordered characteristic functions, $\chi_A^{\rho_{S_x I_y}}(\boldsymbol{\zeta}^*, \boldsymbol{\zeta})$ and $\chi_A^{\rho_{S_y I_x}}(\boldsymbol{\zeta}^*, \boldsymbol{\zeta})$, from equations (6) and (7), respectively, are the Fourier transforms of the normally ordered forms of their associated density operators. Thus, these density operators can be recovered from the operator-valued inverse Fourier transforms,

$$\hat{\rho}_{S_x I_y} = \int \frac{d^2 \zeta_S}{\pi} \int \frac{d^2 \zeta_I}{\pi} \chi_A^{\rho_{S_x I_y}}(\boldsymbol{\zeta}^*, \boldsymbol{\zeta}) e^{-\zeta_S \hat{a}_{S_x}^\dagger - \zeta_I \hat{a}_{I_y}^\dagger} e^{\zeta_S^* \hat{a}_{S_x} + \zeta_I^* \hat{a}_{I_y}}, \tag{A.1}$$

and

$$\hat{\rho}_{S_y I_x} = \int \frac{d^2 \zeta_S}{\pi} \int \frac{d^2 \zeta_I}{\pi} \chi_A^{\rho_{S_y I_x}}(\boldsymbol{\zeta}^*, \boldsymbol{\zeta}) e^{-\zeta_S \hat{a}_{S_y}^\dagger - \zeta_I \hat{a}_{I_x}^\dagger} e^{\zeta_S^* \hat{a}_{S_y} + \zeta_I^* \hat{a}_{I_x}}. \tag{A.2}$$

The reduced density operator $\hat{\rho}_{S_x}$ can be found by first obtaining the reduced anti-normally ordered characteristic function via

$$\chi_A^{\rho_{S_x}}(\zeta_S^*, \zeta_S) = \chi_A^{\rho_{S_x I_y}}(\boldsymbol{\zeta}^* \boldsymbol{\zeta})|_{\zeta_I = 0} = e^{-(1+\bar{n})|\zeta_S|^2}, \tag{A.3}$$

and then performing the operator-valued inverse Fourier transform to obtain

$$\hat{\rho}_{S_x} = \int \frac{d^2 \zeta}{\pi} \chi_A^{\rho_{S_x}}(\zeta^*, \zeta) e^{-\zeta \hat{a}_{S_x}^\dagger} e^{\zeta^* \hat{a}_{S_x}}. \tag{A.4}$$

Similarly, we have that

$$\chi_A^{\rho_{S_y}}(\zeta^*, \zeta) = \chi_A^{\rho_{I_x}}(\zeta^*, \zeta) = \chi_A^{\rho_{I_y}}(\zeta^*, \zeta) = e^{-(1+\bar{n})|\zeta|^2}, \tag{A.5}$$

from which $\hat{\rho}_{S_y}$, $\hat{\rho}_{I_x}$ and $\hat{\rho}_{I_y}$ can be found as in equation (A.4).

We now observe that

$$\chi_A^{\rho_{k_j}}(\zeta^*, \zeta) = \frac{\pi p_{k_j}(\zeta)}{1 + \bar{n}}, \qquad \text{for } k = S, I \text{ and } j = x, y, \tag{A.6}$$

where $p_{k_j}(\zeta)$ is the classical probability density for a zero-mean, complex-valued Gaussian random variable ζ whose second moments are $\langle |\zeta|^2 \rangle_{p_{k_j}} = 1/(1 + \bar{n})$ and $\langle \zeta^2 \rangle_{p_{k_j}} = 0$. We also have that

$$\chi_A^{\rho_{S_x I_y}}(\boldsymbol{\zeta}^*, \boldsymbol{\zeta}) = \frac{\pi^2 p_{S_x I_y}(\boldsymbol{\zeta})}{(1 + \bar{n})^2 - \tilde{n}^2}, \tag{A.7}$$

where $p_{S_x I_y}(\boldsymbol{\zeta})$ is the classical probability density for a zero-mean, complex-valued Gaussian random vector $\boldsymbol{\zeta}^T = [\,\zeta_S \quad \zeta_I\,]$ whose second-moment matrices are

$$\langle \boldsymbol{\zeta} \boldsymbol{\zeta}^\dagger \rangle_{p_{S_x I_y}} = \boldsymbol{\Lambda}_{\text{OPA}} \equiv \frac{1}{(1 + \bar{n})^2 - \tilde{n}^2} \begin{bmatrix} 1 + \bar{n} & 0 \\ 0 & 1 + \bar{n} \end{bmatrix}, \tag{A.8}$$

and

$$\langle \boldsymbol{\zeta} \boldsymbol{\zeta}^T \rangle_{p_{S_x I_y}} = \tilde{\boldsymbol{\Lambda}}_{\text{OPA}} \equiv \frac{1}{(1 + \bar{n})^2 - \tilde{n}^2} \begin{bmatrix} 0 & \tilde{n} \\ \tilde{n} & 0 \end{bmatrix}. \tag{A.9}$$

Similarly, we have that

$$\chi_A^{\rho_{S_y I_x}}(\boldsymbol{\zeta}^*, \boldsymbol{\zeta}) = \frac{\pi^2 p_{S_y I_x}(\boldsymbol{\zeta})}{(1+\bar{n})^2 - \tilde{n}^2}, \tag{A.10}$$

where $p_{S_y I_x}(\boldsymbol{\zeta})$ is the classical probability density for a zero-mean, complex-valued Gaussian random vector $\boldsymbol{\zeta}^T = [\,\zeta_S \quad \zeta_I\,]$ whose second-moment matrices are $\langle \boldsymbol{\zeta}\boldsymbol{\zeta}^\dagger \rangle_{p_{S_y I_x}} = \boldsymbol{\Lambda}_{\text{OPA}}$, and $\langle \boldsymbol{\zeta}\boldsymbol{\zeta}^T \rangle_{p_{S_y I_x}} = -\tilde{\boldsymbol{\Lambda}}_{\text{OPA}}$. With these results in hand, we can readily find that

$$_{k_j}\langle 0|\hat{\rho}_{k_j}|0\rangle_{k_j} = \int \frac{\mathrm{d}^2\zeta_k}{1+\bar{n}}\, p_{k_j}(\zeta_k) = \frac{1}{1+\bar{n}}, \qquad \text{for } k = S, I \text{ and } j = x, y, \tag{A.11}$$

and

$$_{S_x}\langle 0|_{I_y}\langle 0|\hat{\rho}_{S_x I_y}|0\rangle_{I_y}|0\rangle_{S_x} = \iint \frac{\mathrm{d}^2\zeta_S\,\mathrm{d}^2\zeta_I}{(1+\bar{n})^2 - \tilde{n}^2}\, p_{S_x I_y}(\boldsymbol{\zeta}) = \frac{1}{(1+\bar{n})^2 - \tilde{n}^2}, \tag{A.12}$$

$$_{S_y}\langle 0|_{I_x}\langle 0|\hat{\rho}_{S_y I_x}|0\rangle_{I_x}|0\rangle_{S_y} = \iint \frac{\mathrm{d}^2\zeta_S\,\mathrm{d}^2\zeta_I}{(1+\bar{n})^2 - \tilde{n}^2}\, p_{S_y I_x}(\boldsymbol{\zeta}) = \frac{1}{(1+\bar{n})^2 - \tilde{n}^2}. \tag{A.13}$$

Substituting these results into equation (8) yields the dual-OPA configuration's erasure probability,

$$P_{\text{erasure}} = \frac{2}{(1+\bar{n})^2} - \frac{1}{[(1+\bar{n})^2 - \tilde{n}^2]^2}. \tag{A.14}$$

For the success probability, we have that

$$\begin{aligned}
P_{\text{success}} = {}_{SI}\langle\psi^-|\hat{\rho}_{\boldsymbol{SI}}|\psi^-\rangle_{SI} &= \frac{1}{2[(1+\bar{n})^2 - \tilde{n}^2]^2} \\
&\quad \times [\langle(1-|\zeta_S|^2)(1-|\zeta_I|^2)\rangle_{p_{S_x I_y}} + \langle(1-|\zeta_S|^2)(1-|\zeta_I|^2)\rangle_{p_{S_y I_x}} \\
&\quad - 2\,\text{Re}\,(\langle\zeta_S\zeta_I\rangle_{p_{S_x I_y}}\langle\zeta_S^*\zeta_I^*\rangle_{p_{S_y I_x}})] \\
&= \frac{[\bar{n}(1+\bar{n}) - \tilde{n}^2]^2 + 2\tilde{n}^2}{[(1+\bar{n})^2 - \tilde{n}^2]^4}, \tag{A.15}
\end{aligned}$$

where the second equality follows from equations (A.1) and (A.2), and the third from the moment-factoring theorem for complex-valued Gaussian random variables.

A.2. DPA source teleportation

Derivation of the erasure and success probabilities for DPA source teleportation closely parallels what we have just described for the dual-OPA case. The anti-normally ordered characteristic function $\chi_A^{\rho_{S_x I_x S_y I_y}}(\boldsymbol{\zeta}^*, \boldsymbol{\zeta})$ from equation (11) satisfies

$$\chi_A^{\rho_{S_x I_x S_y I_y}}(\boldsymbol{\zeta}^*, \boldsymbol{\zeta}) = \frac{\pi^4}{(1+\bar{n})^2 - \tilde{n}^2} p_{S_x I_x S_y I_y}(\boldsymbol{\zeta}), \tag{A.16}$$

where $p_{S_x I_x S_y I_y}(\boldsymbol{\zeta})$ is the classical probability density function for a zero-mean, complex-valued Gaussian random vector $\boldsymbol{\zeta}^T = [\,\zeta_{S_x} \quad \zeta_{I_x} \quad \zeta_{S_y} \quad \zeta_{I_y}\,]$ whose second-moment matrices are

$$\langle \boldsymbol{\zeta}\boldsymbol{\zeta}^\dagger \rangle_{p_{S_x I_x S_y I_y}} = \begin{bmatrix} \boldsymbol{\Lambda}_{\text{DPA}} & \mathbf{0} \\ \mathbf{0} & \boldsymbol{\Lambda}_{\text{DPA}} \end{bmatrix}, \tag{A.17}$$

Institute *of* **Physics** ⬥ DEUTSCHE PHYSIKALISCHE GESELLSCHAFT

and

$$\langle \boldsymbol{\zeta}\boldsymbol{\zeta}^T \rangle_{p_{S_x I_x S_y I_y}} = \begin{bmatrix} \mathbf{0} & \tilde{\mathbf{\Lambda}}_{\text{DPA}} \\ \tilde{\mathbf{\Lambda}}_{\text{DPA}} & \mathbf{0} \end{bmatrix}, \tag{A.18}$$

with

$$\mathbf{\Lambda}_{\text{DPA}} \equiv \frac{1}{2[(1+\bar{n})^2 - \tilde{n}^2]} \begin{bmatrix} (1+\bar{n})(2+\bar{n}) - \tilde{n}^2 & -\bar{n}(1+\bar{n}) + \tilde{n}^2 \\ -\bar{n}(1+\bar{n}) + \tilde{n}^2 & (1+\bar{n})(2+\bar{n}) - \tilde{n}^2 \end{bmatrix}, \tag{A.19}$$

and

$$\tilde{\mathbf{\Lambda}}_{\text{DPA}} \equiv \frac{1}{2[(1+\bar{n})^2 - \tilde{n}^2]} \begin{bmatrix} \tilde{n} & \tilde{n} \\ \tilde{n} & \tilde{n} \end{bmatrix}. \tag{A.20}$$

We shall also need the reduced anti-normally ordered characteristic functions,

$$\chi_A^{\rho_{k_x k_y}}(\boldsymbol{\zeta}^*, \boldsymbol{\zeta}) = e^{-(1+\bar{n}/2)(|\zeta_{k_x}^2| + |\zeta_{k_y}|^2) + \tilde{n}\,\text{Re}\,(\zeta_{k_x}\zeta_{k_y})} \tag{A.21}$$

$$= \frac{\pi^2}{(1+\bar{n}/2)^2 - (\tilde{n}/2)^2} p_{k_x k_y}(\boldsymbol{\zeta}), \qquad \text{for } k = S, I, \tag{A.22}$$

where $p_{k_x k_y}(\boldsymbol{\zeta})$ is the classical probability density function for a zero-mean, complex-valued Gaussian random vector $\boldsymbol{\zeta}^T = \begin{bmatrix} \zeta_{k_x} & \zeta_{k_y} \end{bmatrix}$ whose second-moment matrices are

$$\mathbf{\Lambda}_{p_{k_x k_y}} = \frac{1}{(1+\bar{n}/2)^2 - (\tilde{n}/2)^2} \begin{bmatrix} 1+\bar{n}/2 & 0 \\ 0 & 1+\bar{n}/2 \end{bmatrix}, \tag{A.23}$$

and

$$\tilde{\mathbf{\Lambda}}_{p_{k_x k_y}} = \frac{1}{(1+\bar{n}/2)^2 - (\tilde{n}/2)^2} \begin{bmatrix} 0 & \tilde{n}/2 \\ \tilde{n}/2 & 0 \end{bmatrix}. \tag{A.24}$$

Using operator-valued inverse Fourier transforms to obtain the necessary density operators and employing the properties of Gaussian probability densities, we then find that

$$P_{\text{erasure}} = \frac{2}{(1+\bar{n}/2)^2 - (\tilde{n}/2)^2} - \frac{1}{(1+\bar{n})^2 - \tilde{n}^2}, \tag{A.25}$$

for the DPA system's erasure probability, and

$$P_{\text{success}} = \frac{[\bar{n}(1+\bar{n}) - \tilde{n}^2]^2 + \tilde{n}^2}{2[(1+\bar{n})^2 - \tilde{n}^2]^3}, \tag{A.26}$$

for its success probability.

A.3. GHZ-state communication

Our final task will be to outline derivations for the erasure and success probabilities of the GHZ-state communication architectures shown in figure 8. Once again, the approach involves anti-normally ordered characteristic functions, operator-valued inverse Fourier transforms and complex-Gaussian moment factoring. Having illustrated most of the details in the dual-OPA and DPA teleportation calculations, we shall content ourselves with a brief summary of how the corresponding calculations are performed for GHZ-state communication.

Consider the dual-DPA architecture from figures 8(*a*), (*b*). The anti-normally ordered characteristic function for $\{\hat{a}_{T_y}(T_c), \hat{\boldsymbol{a}}_1(T_c), \hat{\boldsymbol{a}}_2(T_c), \hat{\boldsymbol{a}}_3(T_c)\}$—the $\hat{y}$-polarized mode of the

trigger memory and the $\hat{x}$- and $\hat{y}$-polarized modes of the three external memories at the end of a loading interval—can be shown to be

$$
\begin{aligned}
\chi_A^{\rho_{T_y}\mathbf{123}}(\boldsymbol{\zeta}^*, \boldsymbol{\zeta}) = {} & \mathrm{e}^{-(1+\bar{n})(|\zeta_{1_x}+\zeta_{2_y}|^2+|\zeta_{1_y}+\zeta_{3_y}|^2)/2+\tilde{n}\,\mathrm{Re}\,[(\zeta_{1_x}+\zeta_{2_y})(\zeta_{1_y}+\zeta_{3_y})]} \\
& \times \mathrm{e}^{-(1+\bar{n})(|\zeta_{T_y}|^2+|\zeta_{2_x}+\zeta_{3_x}|^2/2)-\sqrt{2}\tilde{n}\,\mathrm{Re}\,[\zeta_{T_y}(\zeta_{2_x}+\zeta_{3_x})]} \\
& \times \mathrm{e}^{-(|\zeta_{1_x}-\zeta_{2_y}|^2+|\zeta_{1_y}-\zeta_{3_y}|^2+|\zeta_{2_x}-\zeta_{3_x}|^2)/2},
\end{aligned}
\tag{A.27}
$$

where we have assumed that the same fixed and propagation losses are incurred from the dual-DPA to each of the four memories. Note that this is a conservative assumption, in that it apportions the same propagation loss on the source-to-trigger path as is encountered on the long-distance path to the external memories. From this characteristic function, we find the erasure probability by a tedious Venn-diagram accounting for every way in which one or more of the four memories in figures 8(*a*), (*b*) can fail to absorb photons. The result that is obtained is

$$
\begin{aligned}
P_{\text{erasure}} = {} & \frac{1}{1+\bar{n}} + \frac{2}{(1+\bar{n}/2)^2} + \frac{1}{(1+\bar{n}/2)^2 - (\tilde{n}/2)^2} \\
& - \frac{2}{(1+\bar{n})[(1+\bar{n}/2)^2 - (\tilde{n}/2)^2]} - \frac{4}{(1+\bar{n}/2)[(1+\bar{n}/2)(1+\bar{n}) - \tilde{n}^2/2]} \\
& + \frac{2}{[(1+\bar{n}/2)(1+\bar{n}) - \tilde{n}^2/2]^2} + \frac{1}{[(1+\bar{n}/2)^2 - (\tilde{n}/2)^2][(1+\bar{n})^2 - \tilde{n}^2]} \\
& + \frac{1}{(1+\bar{n})[(1+\bar{n})^2 - \tilde{n}^2]} - \frac{1}{[(1+\bar{n})^2 - \tilde{n}^2]^2}.
\end{aligned}
\tag{A.28}
$$

The success probability, $P_{\text{success}} \equiv {}_{T_y}\langle 1|\,{}_{\text{GHZ}}\langle\psi|\hat{\rho}_{T_y\mathbf{123}}|\psi\rangle_{\text{GHZ}}\,|1\rangle_{T_y}$, also follows from the foregoing characteristic function, after a lengthy bout of complex-Gaussian moment factoring that yields

$$
P_{\text{success}} = \frac{\{[\bar{n}(1+\bar{n}) - \tilde{n}^2]^2 + \tilde{n}^2\}^2}{4[(1+\bar{n})^2 - \tilde{n}^2]^6}.
\tag{A.29}
$$

For the DPA plus the heralded single-photon source, the relevant anti-normally ordered characteristic function is

$$
\begin{aligned}
\chi_A^{\rho\mathbf{123}}(\boldsymbol{\zeta}^*, \boldsymbol{\zeta}) = {} & (1 - \eta|\zeta_{1_x} + \zeta_{2_y}|^2/2)\mathrm{e}^{-|\zeta_{1_x}+\zeta_{2_y}|^2/2} \\
& \times \mathrm{e}^{-(1+\bar{n})(|\zeta_{1_y}+\zeta_{3_y}|^2+|\zeta_{2_x}+\zeta_{3_x}|^2)/2+\tilde{n}\,\mathrm{Re}\,[(\zeta_{1_y}+\zeta_{3_y})(\zeta_{2_x}+\zeta_{3_x})]} \\
& \times \mathrm{e}^{-(|\zeta_{1_x}-\zeta_{2_y}|^2+|\zeta_{1_y}-\zeta_{3_y}|^2+|\zeta_{2_x}-\zeta_{3_x}|^2)/2}.
\end{aligned}
\tag{A.30}
$$

Here we have made the optimistic assumption that the heralded single photon is created in the optimal temporal mode for loading into our trapped-atom quantum memories, but we have tempered this assumption by applying the same loss factor, $\eta \equiv \eta_L \gamma \gamma_c / \Gamma\Gamma_c$, to heralded-photon source-to-memory transmission that applies to DPA-photon source-to-memory transmission. Another round of Venn-diagram accounting, using the preceding anti-normally ordered characteristic function, can now be used to show that the erasure probability for the DPA plus heralded single-photon source GHZ-state architecture is given by

$$
\begin{aligned}
P_{\text{erasure}} = {} & \frac{2-\eta}{1+\bar{n}/2} + \frac{\eta}{(1+\bar{n}/2)^2 - (\tilde{n}/2)^2} \\
& - \frac{2-\eta}{(1+\bar{n}/2)(1+\bar{n}) - \tilde{n}^2/2} + \frac{1-\eta}{(1+\bar{n})^2 - \tilde{n}^2}.
\end{aligned}
\tag{A.31}
$$

Institute *of* **Physics** Φ DEUTSCHE PHYSIKALISCHE GESELLSCHAFT

The success probability for the DPA plus heralded single-photon source system can be obtained from the anti-normally ordered characteristic function by complex-valued Gaussian moment factoring, with the following result:

$$P_{\text{success}} \equiv {}_{\text{GHZ}}\langle\psi|\hat{\rho}_{\mathbf{123}}|\psi\rangle_{\text{GHZ}} = \frac{\eta\{[\bar{n}(1+\bar{n}) - \tilde{n}^2]^2 + \tilde{n}^2\}}{4[(1+\bar{n})^2 - \tilde{n}^2]^3}. \tag{A.32}$$

References

[1] Shapiro J H 2001 Long-distance high-fidelity teleportation using singlet states *Quantum Communication, Measurement, and Computing* vol 3, ed O Hirota and P Tombesi (New York: Kluwer) pp 367–74

[2] Shapiro J H and Wong N C 2000 *J. Opt. B: Quantum Semiclass. Opt.* **2** L1–4

[3] Lloyd S, Shahriar M S, Shapiro J H and Hemmer P R 2001 *Phys. Rev. Lett.* **87** 167903

[4] Bouwmeester D, Pan J-W, Daniell M, Weinfurter H and Zeilinger A 1999 *Phys. Rev. Lett.* **82** 1345–9

[5] Hillery M, Buzek V and Berthiaume A 1999 *Phys. Rev.* A **59** 1829–34

[6] Bennett C H, Brassard G, Crépeau C, Jozsa R, Peres A and Wootters W K 1993 *Phys. Rev. Lett.* **70** 1895–9

[7] Bouwmeester D, Pan J-W, Mattle K, Eibl M, Weinfurter H and Zeilinger A 1997 *Nature* **390** 575–9

[8] Bouwmeester D, Mattle K, Pan J-W, Weinfurter H, Zeilinger A and Zukowski M 1998 *Appl. Phys.* B **67** 749–52

[9] Kumar P 1990 *Opt. Lett.* **15** 1476–8

[10] Huang J M and Kumar P 1992 *Phys. Rev. Lett.* **68** 2153–6

[11] Bergman K, Doerr C R, Haus H A and Shirasaki M 1993 *Opt. Lett.* **18** 643–5

[12] Wong N C, Leong K W and Shapiro J H 1990 *Opt. Lett.* **15** 891–3

[13] Kuklewicz C E, Keskiner E, Wong F N C and Shapiro J H 2002 A High-flux entanglement source based on a doubly-resonant optical parametric amplifier *J. Opt. B: Quantum Semiclass. Opt.* **4** S162–8

[14] Greenberger D M, Horne M A and Zeilinger A 1989 Going beyond Bell's theorem *Bell's Theorem, Quantum Theory, and Conceptions of the Universe* ed M Kafatos (Dordrecht: Kluwer) pp 73–6

[15] Santori C, Pelton M, Solomon G, Dale Y and Yamamoto Y 2000 *Phys. Rev. Lett.* **86** 1502–5